Local and Global Structural Effects of Doping on Ionic Conductivity in Na_3SbS_4 Solid Electrolyte

Cheng-Wei Lee,[†] Mayu Maegawa,[‡] Hirofumi Akamatsu,[‡] Katsuro Hayashi,[‡] Saneyuki Ohno,[*,‡,¶] and Prashun Gorai[*,†,§]

†*Colorado School of Mines, Golden, CO 80401, USA*

‡*Kyushu University, Fukuoka 819-0395, Japan*

¶*Tohoku University, Miyagi 980-8577, Japan*

§*Rensselaer Polytechnic Institute, Troy, NY 12180, USA*

E-mail: saneyuki.ohno.c8@tohoku.ac.jp; goraip@rpi.edu

Abstract

Among Na-ion solid electrolytes, Na_3SbS_4 has achieved high ionic conductivity (σ_{ion}) exceeding 10 mS/cm through aliovalent doping. σ_{ion} enhancement due to aliovalent doping is qualitatively explained by the increase in the concentration of defects that mediate ion diffusion. However, a rigorous atomic-scale mechanistic explanation is needed. Doping also affects σ_{ion} by modifying ion mobility – an effect that is not well understood and often overlooked. We use first-principles defect calculations to mechanistically explain and quantify the increase/decrease in Na vacancy concentration due to aliovalent doping of Na_3SbS_4. By focusing on isovalent doping, we reveal local and global structural effects of doping on the migration barrier, and therefore, ion mobility. In conjunction with experiments, we demonstrate the interplay between the local and

global effects. Doping with heavier anions to achieve more polarizable frameworks is a common approach to enhancing σ_{ion}. Our findings present a unique approach to enhancing σ_{ion} by doping with smaller and lighter cations that form stiffer bonds with anions, which in turn soften the parent framework.

Prior to the development of Li-ion technology in the 1990s, Na-ion batteries were the focus of the research community.[1] Na-ion battery technology offers tremendous potential due to the abundance, cost effectiveness, and suitable redox potential of sodium.[2,3] While the deployment of Na-ion batteries in transportation and portable devices is limited by lower energy/power density compared to their Li-ion counterpart, lower material cost makes Na-ion batteries more suited for grid-scale storage.[2] All-solid-state-batteries containing inorganic solid electrolytes (SEs) are safer and have higher energy/power density compared to current Li-ion technology that uses liquid organic electrolytes.[4] Yet, SEs suffer from low ionic conductivity (σ_{ion}) and limited (electro)chemical stability that have impeded their commercialization. σ_{ion} of SEs must be increased to be competitive with liquid electrolytes ($\sigma_{ion} \sim 10^{-2}$ S/cm) while ensuring electrochemical stability with metal anodes and high-voltage cathodes.[5–8]

Among Na-ion SEs, Na_3SbS_4 has a room-temperature σ_{ion} of around 10^{-3} S/cm.[9–11] Tungsten (W) doping increases σ_{ion} of Na_3SbS_4 above 10^{-2} S/cm.[12–14] σ_{ion} is the product of the mobile ion defect concentration n, ion mobility μ, and electronic charge e – a constant. Mathematically, $\sigma_{ion} = n\mu e$. It has been *qualitatively* shown that aliovalent doping with W increases the concentration of Na vacancies that mediate Na-ion diffusion, i.e., doping increases n.[15,16] However, doping also affects the mobility of Na ions by modifying their migration barrier (ΔE_m), but such effects are not fully understood for doped-Na_3SbS_4.

In this work, we use first-principles defect calculations to *quantitatively* demonstrate the increase/decrease in Na vacancy concentration due to aliovalent doping of Na_3SbS_4. In conjunction with experiments, we reveal local and global structural effects of doping on

ΔE_m. These effects and their interplay manifest even in the case of isovalent doping where doping does not change the mobile ion concentration. We computationally probe 8 different dopants – 5 aliovalent (W, Mo, Si, Ge, Sn) and 3 isovalent (V, Nb, Ta). We compare our computational predictions with existing experimental literature on aliovalent dopants. The complementary experiments in this study focus on isovalent doping.

First, we focus on the aliovalent doping of Na_3SbS_4. Prior experimental studies have considered W, Mo, Si, Ge, and Sn as aliovalent dopants for Na_3SbS_4.[11–13,17] We use first-principles defect calculations to determine the formation energy ($\Delta E_{D,q}$) of substitutional dopants in tetragonal Na_3SbS_4. While it is claimed that tungsten doping induces a phase transition from the tetragonal to the cubic structure,[13] careful measurements have shown that the local structure remains tetragonal.[15] Since Sb is nominally a 5+ cation in Na_3SbS_4, substitutional W^{6+} and Mo^{6+} would be donor dopants while Si^{4+}, Ge^{4+}, and Sn^{4+} are acceptor dopants. Figs. 1(a) and 1(b) show the calculated $\Delta E_{D,q}$ of native defects (V_{Na}, V_{Sb}, V_S, Na_{Sb}, Sb_{Na}, Na_S, S_{Na}, S_{Sb}, Sb_S, Na_i) at a set of elemental chemical potentials that represent four-phase equilibrium in the Na-Sb-S-dopant quaternary chemical space (vertex V5, Table S2–6). $\Delta E_{D,q}$ of native defects are taken from our previous work (Ref. 11) where we showed that Na vacancies (V_{Na}) mediate Na-ion diffusion in Na_3SbS_4. For clarity, only the native defects with low $\Delta E_{D,q}$ are labelled; the four-phase equilibrium is chosen to be consistent with our previous work for undoped Na_3SbS_4.[11]

We find that W and Mo are effective donor defects, as evidenced by the low $\Delta E_{D,q}$ of substitutional W_{Sb} and Mo_{Sb} (Fig. 1a). The self-consistently determined equilibrium Fermi energy, $E_{F,eq}$, which is the relevant Fermi energy is evaluated at 873 K – synthesis temperature of Na_3SbS_4 (see Methods for details). In undoped (or self-doped) Na_3SbS_4, $E_{F,eq}$ is mainly determined by acceptor V_{Na}^{-1} and donor V_{Sb}^{+1}. Doping with W and Mo shifts the $E_{F,eq}$ closer to the conduction band, i.e., n-type doping, by 0.36 and 0.16 eV, respectively, relative to the undoped case. Consequently, $\Delta E_{D,q}$ of V_{Na}^{-1} is lowered. Fig. 1c shows that V_{Na}^{-1} concentration increases by approx. 150 and 10 times due to W and Mo doping, respectively.

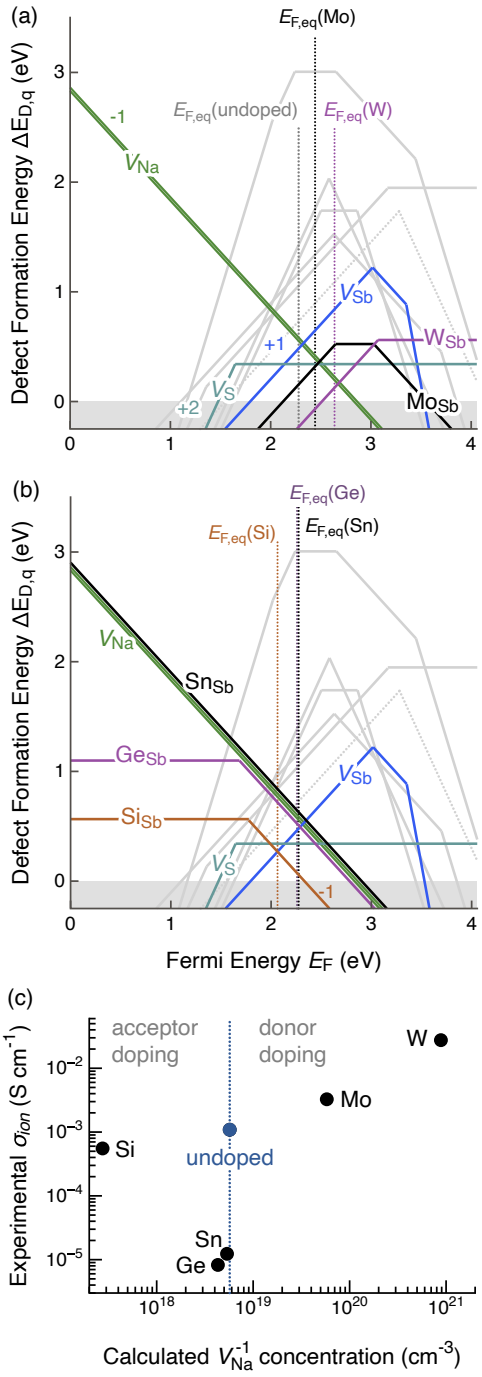

Figure 1: Formation energy of relevant native defects and substitutional dopants in Na_3SbS_4. (a) donor dopants – W and Mo, and (b) acceptor dopants – Si, Ge, and Sn. Equilibrium Fermi energy, $E_{F,eq}$, is calculated at 823 K. (c) Experimentally measured ionic conductivity (σ_{ion})[11–13,17] vs. calculated V_{Na}^{-1} concentration for W, Mo, Si, Ge, and Sn doping.

Our computational prediction is consistent with the experimentally observed increase in σ_{ion} (Fig. 1c). Assuming no change in Na ion mobility due to doping, the increased V_{Na}^{-1}

concentration should translate to a linearly proportional increase in σ_{ion}. However, measured σ_{ion} increases by only 30 and 3 times due to W and Mo doping, suggesting additional doping effects are at play that diminish the impact of V_{Na}^{-1} concentration increase. Dopants most likely also affect the migration barrier and therefore, the mobility of Na ions. We explore this effect in more detail later in this study.

Our defect calculations confirm that Si, Ge, and Sn act as acceptor dopants, i.e., p-type dopants, which shift $E_{\mathrm{F,eq}}$ towards the valence band and increases $\Delta E_{D,q}$ of V_{Na}^{-1} (Fig. 1b). We find that substitutional Si ($\mathrm{Si_{Sb}}$) has the lowest $\Delta E_{D,q}$ followed by Ge and Sn. Si doping shifts $E_{\mathrm{F,eq}}$ by 0.21 eV, which lowers V_{Na}^{-1} concentration by 20 times relative to the undoped case (Fig. 1c). Experimentally, σ_{ion} decreases by 2 times when doped with Si. Since $\Delta E_{D,q}$ of $\mathrm{Ge_{Sb}}$ and $\mathrm{Sn_{Sb}}$ are comparable or even slightly higher than V_{Na}^{-1}, we predict that Ge and Sn doping will have minimal effect on V_{Na}^{-1} concentration. However, measured σ_{ion} is found to decrease dramatically by almost 2 orders of magnitude, again suggesting that doping effects beyond changes in the mobile ion concentration are at play.

To understand how doping affects σ_{ion} beyond changing the mobile ion concentration, we probe three transition elements (V, Nb, Ta) that exist in +5 oxidation state. Being redox active, these transition elements also exist in other oxidation states. The hypothesis is that V, Nb, and Ta in their +5 oxidation state isoelectronically substitute on Sb site, and affect σ_{ion} of $\mathrm{Na_3SbS_4}$ by modifying the ion mobility (e.g., by altering migration barrier) alone. By keeping the mobile ion concentration unchanged, isovalent doping allows us to deconvolute doping effects on the mobile ion concentration and mobility. We perform defect and migration barrier calculations in conjunction with experiments to elucidate these effects.

First, we computationally check if V, Nb, and Ta are isovalent dopants with high solubility in $\mathrm{Na_3SbS_4}$. Fig. S1 presents $\Delta E_{D,q}$ of substitutional $\mathrm{V_{Sb}}$, $\mathrm{Nb_{Sb}}$, and $\mathrm{Ta_{Sb}}$. We consider -1, 0, and 1 charge states of these defects, but find that the neutral charge state to be the most stable at E_{F} across the band gap. In addition, $\Delta E_{D,q}$ of $\mathrm{Nb_{Sb}}$ and $\mathrm{Ta_{Sb}}$ is small ($\lesssim 0.05$ eV) suggesting high solubility of Nb and Ta on the Sb site. While $\Delta E_{D,q}$ of $\mathrm{V_{Sb}}$ is higher than

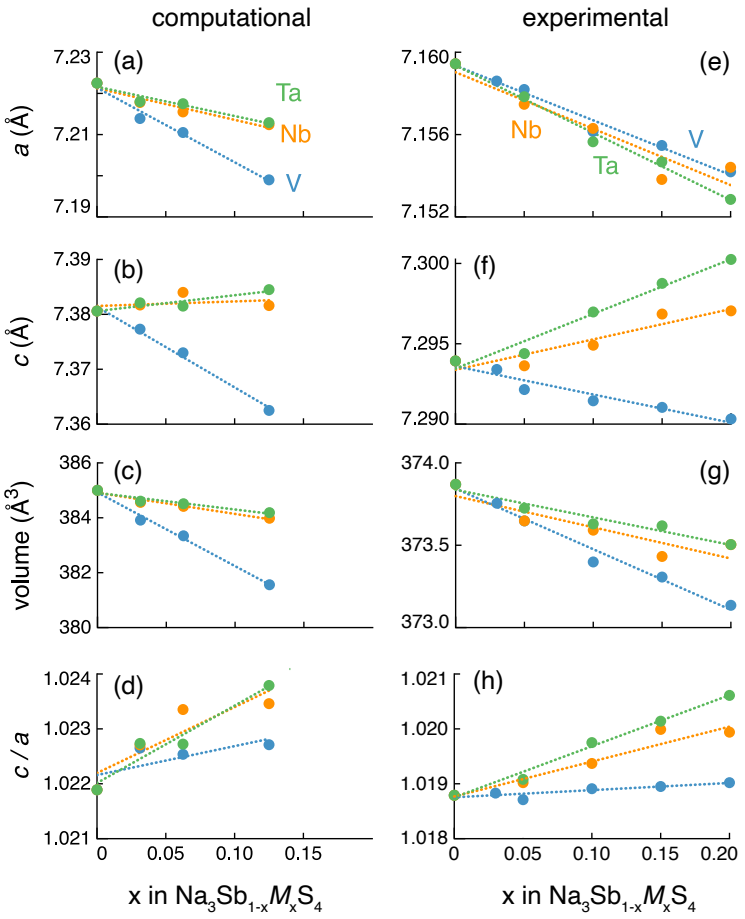

Figure 2: Computed and measured lattice parameters (a, c), cell volume, and lattice parameter ratio c/a as a function of composition x in $Na_3Sb_{1-x}M_xS_4$ (M = V, Nb, Ta).

Nb and Ta, it is still small ∼0.38 eV. Our defect calculations point to the high solubility of isovalent V, Nb, and Ta substitution in tetragonal Na_3SbS_4, which is consistent with the reported synthesis of fully-substituted tetragonal Na_3VS_4,[18] orthorhombic Na_3NbS_4,[19] and orthorhombic Na_3TaS_4.[20] The fully-substituted versions all feature Na ions and MS_4 tetrahedra (M = V, Nb, Ta). Motivated by these findings, we synthesized $Na_3Sb_{1-x}M_xS_4$ (M = V, Nb, Ta) samples via solid-state reaction (see Methods). To avoid complications associated with phase change (e.g., tetragonal → orthorhombic), we consider compositions with x up to 0.2.

Fig. 2 presents the calculated and measured changes in the lattice parameters (a, c), unit-cell volume, and c/a as a function of the composition (x). Lattice parameters and volume

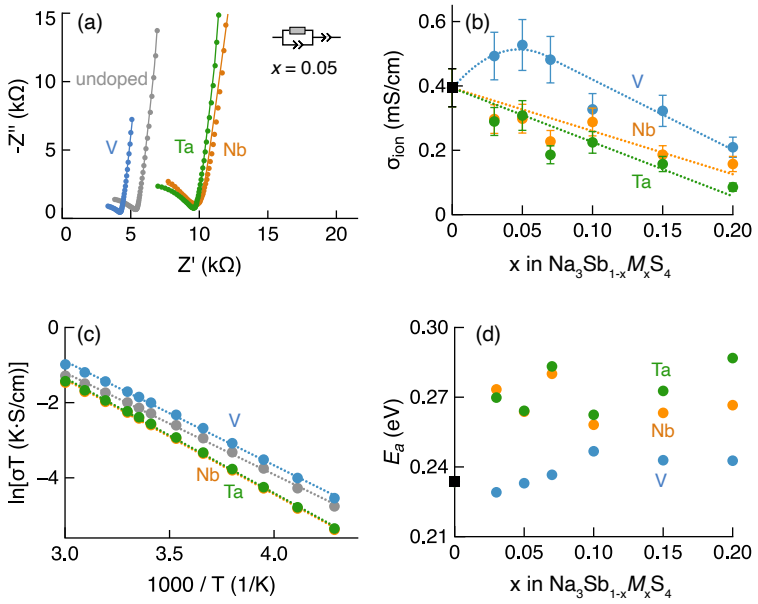

Figure 3: (a) Nyquist plot measured at -40°C for $Na_3Sb_{1-x}M_xS_4$ with $x = 0.05$ (M = V, Nb, Ta). (b) ionic conductivity at room temperature as a function of x. (c) Arrhenius plot based on the total resistance for $x = 0.05$, shown in (a). (d) measured activation energy as a function of x. Values of undoped samples are shown as black squares.

change almost linearly with x following Vegard's law, which confirms the incorporation of V, Nb , and Ta in tetragonal Na_3SbS_4. Generally, the computed trends are consistent with the experimental measurements, although the computed parameters are larger than the measured values because of the well-known underbinding with GGA exchange-correlation functional. Nonetheless, the computed a, c, and volume for Na_3SbS_4 are overestimated by ∼0.9%, ∼1.2%, and ∼3.0%, respectively, which are typical errors with GGA functional. The observed changes are also consistent with the ionic radii. V^{5+} is significantly smaller than Sb^{5+} while Ta^{5+} is similar in size to Sb^{5+}; consequently, V (Ta) incorporation causes the largest (smallest) change in a and volume. However, c slightly increases with Nb and Ta doping, and as a result, c/a also increases, indicating an increase in the tetragonality. Again, this behavior is consistent with experimental measurements. The changes in lattice parameters alone provide early indications that V doping is likely to behave differently from Nb and Ta doping.

We use temperature-dependent impedance spectroscopy to study the effect of isovalent

doping on σ_{ion} of $Na_3Sb_{1-x}M_xS_4$. The representative data obtained at -40° C is shown in the Nyquist plot in Fig. 3(a). The spectra obtained from all samples could be fitted by a parallel circuit consisting of one resistor representing the ion resistance, one constant phase element (CPE), its capacitive component, and a CPE in series with it, representing the ion-blocking behavior. As with other sulfide solid electrolytes, we were unable to separate the bulk and grain boundary contributions even at -40 ℃ but the capacitances of the ion transport part obtained from the fit were 5-15 pF, indicating that the data reflects the bulk contribution,[21] i.e., the effect of the substituted elements in the structure. Fig. 3(b) shows the measured σ_{ion} at room temperature for compositions $x \leq 0.2$. σ_{ion} of undoped Na_3SbS_4 is 0.4 mS/cm, which is consistent with our prior results under the most Na-rich synthesis condition.[11] Na-ion diffusion slows down with increasing tetragonality (c/a),[22,23] which we observe for Nb and Ta doping (Figs. 2d, 2e). Indeed, we observe a monotonic decrease in σ_{ion} with increasing Nb and Ta doping in Fig. 3(b). However, we observe non-monotonic effect of V doping on σ_{ion}, with σ_{ion} first increasing (up to $x \sim 0.05$) and then decreasing in a manner similar to Nb and Ta. This interesting non-monotonic change in σ_{ion} cannot be simply described by differences in the ionic radii of the dopants relative to Sb, but it is an indication of competing factors at play. Figs. 3(c) and 3(d) show the Arrhenius temperature-dependence of σ_{ion} for $x = 0.05$ and the comparison of the activation energies (obtained from the Arrhenius dependence) across all samples, respectively. Similar Arrhenius dependence implies the ion diffusion mechanism remains unchanged due to V, Nb, and Ta doping. We notice a slight increase in the activation energy for Nb- and Ta-doped samples, but remains virtually unchanged for V doping. Next, we elucidate the local and global structural effects of doping on σ_{ion} and derive materials design rules for solid electrolyte doping.

Doping affects the energy landscape for ion migration in two distinct ways. Firstly, the migrating ion locally interacts with the dopant, which will change the ion migration barrier (ΔE_m). Secondly, doping changes the global structural properties such as the cell volume, which in turn changes ΔE_m. To quantity the local and global effects, we calculate ΔE_m

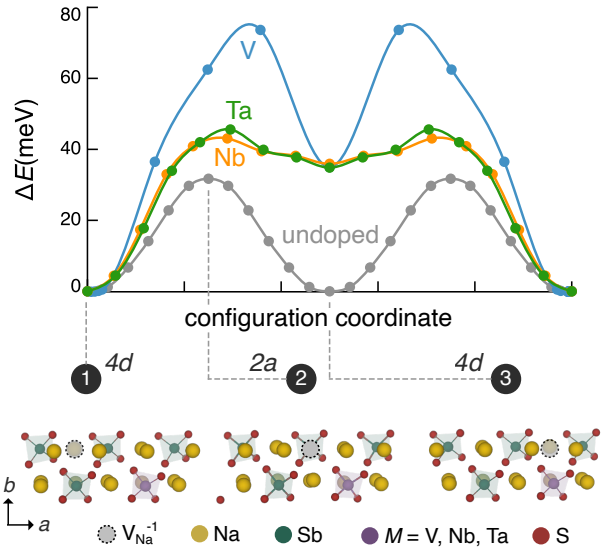

Figure 4: Migration barrier of Na ions mediated by Na vacancy (V_{Na}^{-1}) in undoped and M-doped Na_3SbS_4 (M = V, Nb, and Ta) along the a axis. The structures along the migration pathway are shown, with positions 1 and 3 corresponding to the *4d* Wyckoff site and 2 corresponding to *2a* site of Na. Na-vacancy mediate diffusion of Na ions follows a concerted mechanism along the a axis. The dopant M is located at the center of the configuration coordinate. The configuration coordinate is normalized using the square root of the sum of squared distances of all atoms between images along the pathway.

for Na-ion migration using the nudged elastic band method (see Methods for details). We model the Na-ion diffusion mediated by charged Na vacancies (V_{Na}^{-1}). Specifically, we focus on Na-ion diffusion along a axis of tetragonal Na_3SbS_4 (∼32 meV, Fig. 4) since ΔE_m along c axis is significantly larger (∼78 meV, Fig. S2). In a tetragonal cell, a and b are equivalent. In a polycrystalline sample, we expect the overall σ_{ion} to be dominated by Na-ion diffusion along a and b (Fig. S2). We also find that Na-ion diffusion along a and b follow a concerted mechanism (Fig. 4), also observed in other solid electrolytes.[24,25]

To fully understand the competing nature of the local and global structural effects, we must deconvolute the two effects. We do so by calculating ΔE_m in two scenarios: (1) Na-ion migrating in the vicinity of the dopants, using undoped Na_3SbS_4 cell parameters, and (2) Na-ion migrating in a cell with volume adjusted to match the doping level (Fig. 2), without explicitly adding the dopant in the cell. The former captures the local structural effects while the latter reflects the global effects.

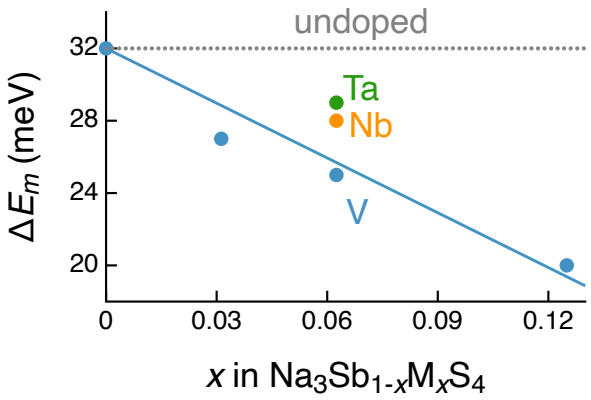

Figure 5: Effect of global structural change (volume contraction due to isovalent substitution of V, Nb, Ta) on migration barrier (ΔE_m) of Na ions along the a axis. V substitution decreases ΔE_m almost linearly with x.

Fig. 4 shows the energy landscape for Na-ion migration in the vicinity of the dopant, which is placed at the location "3" on the configuration coordinate (corresponding position in the structure shown below) and effective conc. is $x = 0.0625$. Doping with V, Nb, and Ta increases ΔE_m by 41.9, 11.4, and 13.9 meV, respectively, compared to undoped Na_3SbS_4, where ΔE_m is 32 meV. In fact, ΔE_m for V doping (74 meV) is comparable to that along c axis in undoped Na_3SbS_4 (78 meV).

Next, to capture the global structural effects of doping, we compute ΔE_m of Na ions in simulation cells that are scaled to match the volume of $Na_3Sb_{1-x}M_xS_4$ (Fig. 2c) without explicitly adding the dopant atoms in the cells. Fig. 5 presents ΔE_m along the a/b axes as a function of the doping level, x. ΔE_m computed in this manner is essentially the Na-ion migration barrier far from the dopant site, where the volume changes affect ΔE_m but direct local interaction with the dopant atom is weak or practically absent. ΔE_m decreases almost linearly with increasing V doping. Nb and Ta doping also decrease ΔE_m (at $x = 0.0625$) relative to undoped Na_3SbS_4 but V doping reduces ΔE_m by 2X compared to Nb and Ta. In summary, our computational results suggest that while ΔE_m *increases* locally in the vicinity of the isovalent dopants, global volume contraction *decreases* ΔE_m. The latter effect will prevail only at low doping concentrations because the local effects will dominate at higher concentrations.

With a quantitative understanding of the two competing factors, we can now, at least qualitatively, explain the observed trends in σ_{ion} as a function of M doping (Fig. 3). Mathematically, $\sigma_{ion} = n\mu e$, where n remains unchanged due to isovalent doping. $\mu = A.e^{-\Delta E_m/k_B T}$, where A is the prefactor that depends on a geometric factor and jump frequency and k_B is the Boltzmann constant. Assuming the prefactor remains unchanged, changes in σ_{ion} due to doping reflects changes in ΔE_m. Here, ΔE_m is an effective migration barrier that includes both local and global effects of doping. For Nb and Ta doping, σ_{ion} consistently decreases with increasing doping concentration since the barrier-reducing global effect is weaker than the local barrier-enhancing effect. For V doping, the barrier-reducing global effect is roughly two times stronger than Nb and Ta, and therefore, we observe an increase in σ_{ion} at low doping concentrations followed by the expected decrease at higher concentrations where the barrier-enhancing local effects dominate.

Zeng et al. reported that local structural distortions give rise to nearly-degenerate potential energy surfaces with low ΔE_m that create ion percolating pathways.[26] Motivated by this idea, we analyze the structural distortions caused by isovalent dopants (Fig. S3). We characterize the structural distortion by calculating the Voronoi volumes of each Na ion in $Na_3Sb_{1-x}M_xS_4$ (M = V, Nb, Ta) for x = 0.03, 0.06, and 0.12. The Voronoi volumes of the two Na Wyckoff sites (*2a*, *4d*) in undoped Na_3SbS_4 are marked with vertical dotted lines in Fig. S3. In doped Na_3SbS_4, there is a distribution of Na Voronoi volumes; the distribution becomes wider with increasing isovalent doping for V, Nb, and Ta. The distributions for V doping are noticeably wider compared to Nb and Ta, indicating greater local structural distortions and possible formation of percolating pathways for Na-ion migration.

We perform Raman spectroscopy to further elucidate the effect of doping on the structural distortions and the vibrational properties. Fig. 6 (top) shows the Raman spectra measured in the vicinity of a symmetric (ν_S) and two asymmetric (ν_a) SbS_4^{3-} stretching modes.[10] SbS_4^{3-} peaks persist even after M doping as the Sb-S sublattice is still predominantly composed of $SbS_4{}^{3-}$. The lower panels in Fig. 6 are the peak positions of $SbS_4{}^{3-}$ vibration modes. We

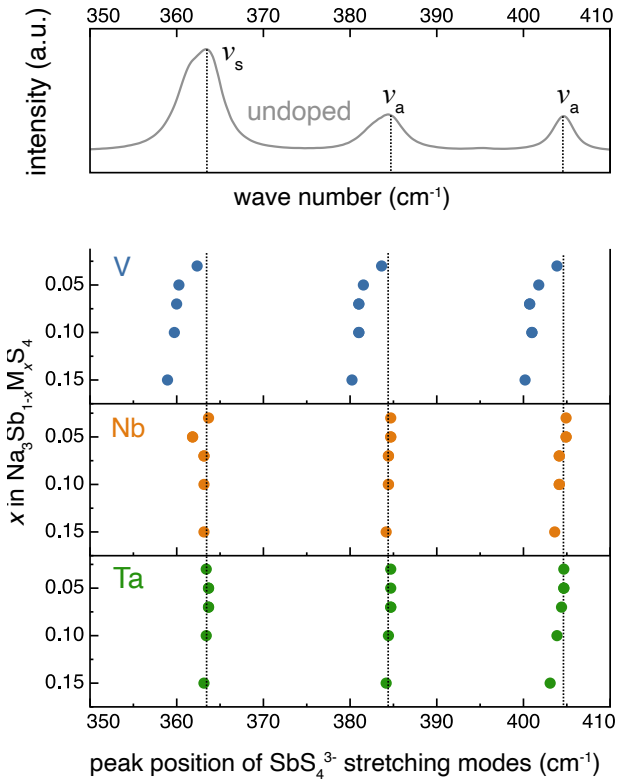

Figure 6: Raman spectra of symmetric (ν_S) and asymmetric (ν_a) SbS_4^{3-} stretching modes in undoped and M-doped Na_3SbS_4 (M = V, Nb, Ta). SbS_4^{3-} stretching modes soften in V-doped Na_3SbS_4 as indicated by the lower wave numbers.

find that the peak positions remain virtually unchanged for Nb and Ta doping, suggesting minimal effect of doping on the vibrational properties of the Sb-S sublattice. V doping causes a noticeable shift in the SbS_4^{3-} vibrational modes to lower wavenumbers, consistent with the larger structural distortions (Fig. S3). In contrast, the VS_4^{3-} vibrational modes appear at wavenumbers larger that SbS_4^{3-}, indicating stiffer V–S bonds. Softening of SbS_4^{3-} stretching modes is likely a result of the chemical pressure generated by the introduction of smaller and lighter V, and stiffer V-S bonds. Softer Sb-S sublattice is more polarizable, which reduces the interaction between the Sb-S framework and migrating Na ions and thereby, boosts σ_{ion}.[27]

In summary, we use first-principles defect calculations to quantify the increase/decrease in Na vacancy concentration due to n- and p-type aliovalent doping of Na_3SbS_4. In addition to changing the concentration of defects that mediate ion diffusion, doping also affects the ion

mobility, mainly by modifying ΔE_m. We perform first-principles defect and migration barrier calculations in conjunction with experiments to mechanistically elucidate the local and global effects of doping on ΔE_m and therefore, σ_{ion}. Doping or alloying with heavier anions to achieve a more polarizable framework is a commonly prescribed approach to enhancing σ_{ion} of solid electrolytes.[28] Our findings highlight an alternative and unique approach to enhancing σ_{ion} by doping with smaller and lighter cations that form stiff bonds with the anion, which in turn softens the parent framework.

Author Contributions

Cheng-Wei Lee: Investigation (equal), Data Curation (equal) , Writing (Original Draft). **Mayu Maegawa**: Investigation (equal), Data Curation (equal), Writing (Editing). **Hirofumi Akamatsu**: Investigation (support), Data Curation (support), Writing (Editing). **Katsuro Hayashi**: Supervision (suppport), Writing (Editing). **Saneyuki Ohno**: Conceptualization (equal), Investigation (equal), Data Curation (equal), Writing (Editing), Supervision (equal). **Prashun Gorai**: Conceptualization (equal), Investigation (equal) , Data Curation (equal), Writing (Editing), Supervision (equal).

Acknowledgements

P.G. acknowledges support from the Laboratory Directed Research and Development (LDRD) program at NREL. The research was performed using computational resources sponsored by the Department of Energy's Office of Energy Efficiency and Renewable Energy and located at the NREL. S.O. gratefully acknowledges Toyota Riken for financial support through a Rising Fellow Program and JSPS KAKENHI Grant Numbers JP23K26762. The synchrotron radiation experiments were performed at the BL02B2 of SPring-8 with the approval of the Japan Synchrotron Radiation Research Institute (JASRI) (proposal nos. 2021B1609 and 2022A1489).

References

(1) Tapia-Ruiz, N.; Armstrong, A. R.; Alptekin, H.; Amores, M. A.; Au, H.; Barker, J.; Boston, R.; Brant, W. R.; Brittain, J. M.; Chen, Y.; others 2021 roadmap for sodium-ion batteries. *Journal of Physics: Energy* **2021**, *3*, 031503.

(2) Palomares, V.; Serras, P.; Villaluenga, I.; Hueso, K. B.; Carretero-González, J.; Rojo, T. Na-ion batteries, recent advances and present challenges to become low cost energy storage systems. *Energy Environ. Sci.* **2012**, *5*, 5884–5901.

(3) Yabuuchi, N.; Kubota, K.; Dahbi, M.; Komaba, S. Research Development on Sodium-Ion Batteries. *Chemical Reviews* **2014**, *114*, 11636–11682.

(4) Janek, J.; Zeier, W. G. A solid future for battery development. *Nature Energy* **2016**, *1*, 16141.

(5) Kato, Y.; Hori, S.; Saito, T.; Suzuki, K.; Hirayama, M.; Mitsui, A.; Yonemura, M.; Iba, H.; Kanno, R. High-power all-solid-state batteries using sulfide superionic conductors. *Nature Energy* **2016**, *1*, 16030.

(6) Bielefeld, A.; Weber, D. A.; Janek, J. Modeling Effective Ionic Conductivity and Binder Influence in Composite Cathodes for All-Solid-State Batteries. *ACS Applied Materials & Interfaces* **2020**, *12*, 12821–12833.

(7) Ohno, S.; Banik, A.; Dewald, G. F.; Kraft, M. A.; Krauskopf, T.; Minafra, N.; Till, P.; Weiss, M.; Zeier, W. G. Materials design of ionic conductors for solid state batteries. *Progress in Energy* **2020**, *2*, 022001.

(8) Ohno, S.; Zeier, W. G. Toward Practical Solid-State Lithium–Sulfur Batteries: Challenges and Perspectives. *Accounts of Materials Research* **2021**, *2*, 869–880.

(9) Wang, H.; Chen, Y.; Hood, Z. D.; Sahu, G.; Pandian, A. S.; Keum, J. K.; An, K.;

Liang, C. An Air-Stable Na3SbS4 Superionic Conductor Prepared by a Rapid and Economic Synthetic Procedure. *Angewandte Chemie* **2016**, *128*, 8693–8697.

(10) Zhang, L.; Zhang, D.; Yang, K.; Yan, X.; Wang, L.; Mi, J.; Xu, B.; Li, Y. Vacancy-Contained Tetragonal Na3SbS4 Superionic Conductor. *Advanced Science* **2016**, *3*, 1600089.

(11) Shimoda, M.; Maegawa, M.; Yoshida, S.; Akamatsu, H.; Hayashi, K.; Gorai, P.; Ohno, S. Controlling Defects to Achieve Reproducibly High Ionic Conductivity in Na_3SbS_4 Solid Electrolytes. *Chemistry of Materials* **2022**, *34*, 5634–5643.

(12) Fuchs, T.; Culver, S. P.; Till, P.; Zeier, W. G. Defect-Mediated Conductivity Enhancements in $Na_{3-x}Pn_{1-x}W_xS_4$ (Pn = P, Sb) Using Aliovalent Substitutions. *ACS Energy Letters* **2020**, *5*, 146–151.

(13) Hayashi, A.; Masuzawa, N.; Yubuchi, S.; Tsuji, F.; Hotehama, C.; Sakuda, A.; Tatsumisago, M. A sodium-ion sulfide solid electrolyte with unprecedented conductivity at room temperature. *Nature Communications* **2019**, *10*, 5266.

(14) TAKAYANAGI, T.; NASU, A.; TSUJI, F.; SAKUDA, A.; TATSUMISAGO, M.; HAYASHI, A. Mechanochemically Prepared Highly Conductive $Na_{2.88}Sb_{0.88}W_{0.12}S_4$-NaI Composite Electrolytes for All-Solid-State Sodium Battery. *Electrochemistry* **2022**, *90*, 047005–047005.

(15) Maus, O.; Agne, M. T.; Fuchs, T.; Till, P. S.; Wankmiller, B.; Gerdes, J. M.; Sharma, R.; Heere, M.; Jalarvo, N.; Yaffe, O.; Hansen, M. R.; Zeier, W. G. On the Discrepancy between Local and Average Structure in the Fast Na+ Ionic Conductor Na2.9Sb0.9W0.1S4. *Journal of the American Chemical Society* **2023**, *145*, 7147–7158.

(16) Jalem, R.; Hayashi, A.; Tsuji, F.; Sakuda, A.; Tateyama, Y. First-Principles Calculation Study of Na^+ Superionic Conduction Mechanism in W- and Mo-Doped Na_3SbS_4 Solid Electrolytes. *Chemistry of Materials* **2020**, *32*, 8373–8381.

(17) Tsuji, F.; Masuzawa, N.; Sakuda, A.; Tatsumisago, M.; Hayashi, A. Preparation and Characterization of Cation-Substituted Na_3SbS_4 Solid Electrolytes. *ACS Applied Energy Materials* **2020**, *3*, 11706–11712.

(18) He, Y.; Lu, F.; Kuang, X. Enhanced sodium ion conductivity in Na_3VS_4 by P-doping. *RSC Adv.* **2019**, *9*, 39180 – 39186.

(19) Niewa, R.; Vajenine, G. V.; DiSalvo, F. J. Synthesis and Crystal Structure of Ternary Sulfides A_3MS_4 with A=Na, Rb and M=Nb, Ta. *Journal of Solid State Chemistry* **1998**, *139*, 404–411.

(20) Herzog, S.; Näther, C.; Dürichen, P.; Bensch, W. Synthesis and Crystal Structure of a New Alkali Metal Tantalum Sulfide: Na_3TaS_4. *Zeitschrift für anorganische und allgemeine Chemie* **1998**, *624*, 2021–2024.

(21) Irvine, J. T. S.; Sinclair, D. C.; West, A. R. Electroceramics: Characterization by Impedance Spectroscopy. *Advanced Materials* **1990**, *2*, 132–138.

(22) Zhang, D.; Cao, X.; Xu, D.; Wang, N.; Yu, C.; Hu, W.; Yan, X.; Mi, J.; Wen, B.; Wang, L.; Zhang, L. Synthesis of cubic Na3SbS4 solid electrolyte with enhanced ion transport for all-solid-state sodium-ion batteries. *Electrochimica Acta* **2018**, *259*, 100–109.

(23) Chaudhary, M.; Pominov, A.; Mumbaraddi, D.; Allen, B.; Meyer, J.; Kirchberger, A. M.; Bernard, G. M.; Nilges, T.; Mar, A.; Michaelis, V. K. Drop That Activation Energy: Tetragonal to Cubic Transformations in $Na_3PS_{4-x}Se_x$ for Solid State Sodium Ion Battery Materials. *Advanced Functional Materials* **2024**, *34*, 2311829.

(24) He, X.; Zhu, Y.; Mo, Y. Origin of fast ion diffusion in super-ionic conductors. *Nature Communications* **2017**, *8*, 15893.

(25) de Klerk, N. J. J.; van der Maas, E.; Wagemaker, M. Analysis of Diffusion in Solid-State Electrolytes through MD Simulations, Improvement of the Li-Ion Conductivity in β-Li3PS4 as an Example. *ACS Appl. Energy Mater.* **2018**, *1*, 3230–3242.

(26) Zeng, Y.; Ouyang, B.; Liu, J.; Byeon, Y.-W.; Cai, Z.; Miara, L. J.; Wang, Y.; Ceder, G. High-entropy mechanism to boost ionic conductivity. *Science* **2022**, *378*, 1320–1324.

(27) Krauskopf, T.; Muy, S.; Culver, S. P.; Ohno, S.; Delaire, O.; Shao-Horn, Y.; Zeier, W. G. Comparing the Descriptors for Investigating the Influence of Lattice Dynamics on Ionic Transport Using the Superionic Conductor $Na3PS_{4-x}Se_x$. *Journal of the American Chemical Society* **2018**, *140*, 14464–14473.

(28) Kraft, M. A.; Culver, S. P.; Calderon, M.; Bocher, F.; Krauskopf, T.; Senyshyn, A.; Dietrich, C.; Zevalkink, A.; Janek, J.; Zeier, W. G. Influence of lattice polarizability on the ionic conductivity in the lithium superionic argyrodites Li6PS5X (X= Cl, Br, I). *Journal of the American Chemical Society* **2017**, *139*, 10909–10918.